We are IntechOpen, the world's leading publisher of Open Access books
Built by scientists, for scientists

6,900
Open access books available

186,000
International authors and editors

200M
Downloads

Our authors are among the

154
Countries delivered to

TOP 1%
most cited scientists

12.2%
Contributors from top 500 universities

CLARIVATE ANALYTICS
BOOK CITATION INDEX
INDEXED

WEB OF SCIENCE™

Selection of our books indexed in the Book Citation Index
in Web of Science™ Core Collection (BKCI)

Interested in publishing with us?
Contact book.department@intechopen.com

Physical Background and Simulation of Creep in Steels

Stan T. Mandziej

Abstract

The simulative accelerated creep test (ACT) was developed as a response to an overall need of gaining in a short time useful physical data for determining long-term behavior of materials exposed to operation under stress at elevated temperatures in power generation and chemical processing industries. Additionally, the recently frequent power plant shutdowns due to adding solar/wind power to the net, call for creep-fatigue data, which standard creep tests cannot provide. In response to these needs, a thermal-mechanical fatigue procedure-ACT-was designed, taking into account physical phenomena causing microstructure transformation during creep, in particular generation of dislocation substructures, their role in nucleation of voids and cracks, intensification of carbide precipitation, and decay of mechanical properties during long-time exposure to elevated temperatures. The actual ACT procedure generates adequate data for calculating true lifetime of the tested creep resisting material for a nominal stress.

Keywords: creep, physical simulation, dislocation substructures, carbide precipitation

1. Introduction

Conventional "constant-load" creep tests of new steels and welds for thermal power generation and chemical processing are very long lasting, thus delaying the application of newly developed steels for years. Even more serious problem appears with creep tests on heat-affected zones in welded joints of these steels, as welding procedure seriously influences the creep properties and the HAZs are very often considered as weakest links of the joints. While most of the design of components and estimation of power plants lifetime is based on long-term creep data, which are generally available for the plate and pipe creep resisting steels, in case of the welded joints on these components, such data are not always easily found, for example, the repair welds are very often not available, especially when repairs were performed outside. To address all these issues, a simulative test was developed allowing to obtain creep life data in less than 24 h. It has been implemented on the Gleeble physical simulator [1]. It is based on detailed observations of microstructural phenomena occurring in martensitic-ferritic steels and welds during exposure to creep. The accelerated creep test is a low-cycle thermal-mechanical fatigue procedure designed to transform the creep resisting steels and welds in the same manner like true creep, only occurring in much shorter time.

2. Physical simulation of creep

Considering creep as a plastic deformation appearing at elevated temperature, with small strains and very small strain rates [2], next to the short duration demanded from the ACT are the following conditions:

1. The basic temperature and applied strains in the ACT must prevent odd transformations like secondary dissolution of carbides or intensive formation of nonequilibrium phases, as well as strain-induced precipitation.

2. The final deformation at fracture, in particular crosswise strain, must be like at real creep-just a few pct in total.

3. The depletion of steel matrix in alloying elements must be achieved similar to that of crept steels, and the carbide phases or other precipitates at onset of cracks must not be different.

4. As creep in the matrix of ferritic-martensitic steels is the phenomenon in which thousands of grains or hundred of thousands of subgrains take part, the portions of samples for ACT that undergo transformation must have adequate "bulk" size, so the first creep voids and cracks in the test nucleate predominantly in most vulnerable sites of microstructure.

Then the simulative test must be in agreement with the following observations:
The creep voids nucleate preferentially at grain boundaries of recrystallized grains or recovered subgrains, in which oriented slip is observed (**Figure 1**), while inside several creep voids, escape of slip lines can be seen (**Figure 2**). Such voids very seldom nucleate at any larger precipitates.

In the substructure of the crept steels, $a/2<111>$ screw dislocations dominate, and these dislocations when not pinned to precipitates are highly mobile. In thin foil of thickness about 260 nm, relatively medium density of such dislocations could be seen (**Figure 3**), while in thicker foil of about 380 nm, their density is much higher, especially when interacting with precipitates and on intersections of two families of these screw dislocations, the $a<001>$ edge dislocations could be identified (**Figure 4**). These last dislocations are mobile with Burgers vectors in {110} planes [3].

When the sample taken from a crept material containing internal "clean" creep voids not exposed to atmosphere is fractured below its ductile-to-brittle transition
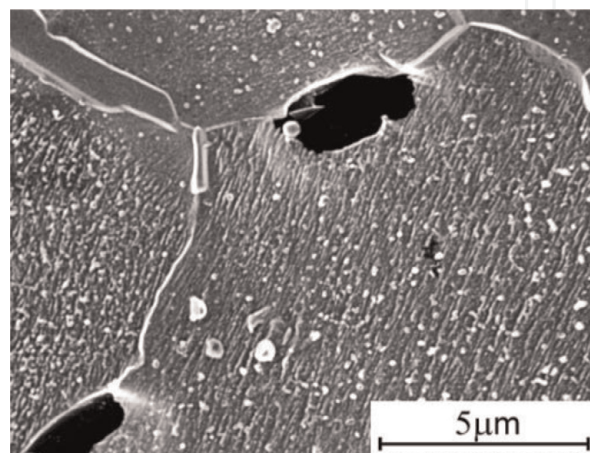

Figure 1.
½ CrMoV steel crept for 22.5 years/16.6 MPa at 568°C; FeCl₃ etched for slip lines, SEM SE-image.
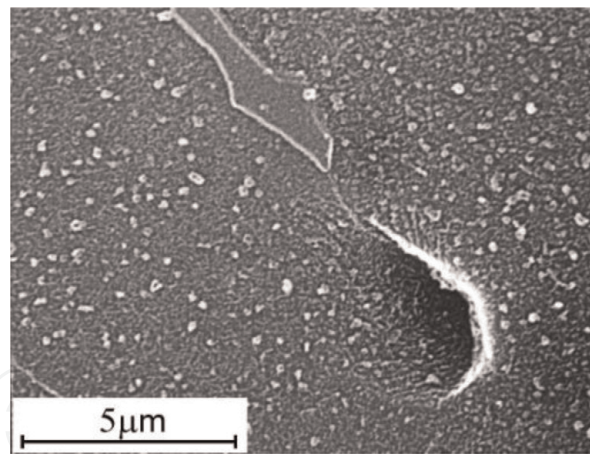
Figure 2.
½ CrMoV steel crept for 22.5 years/16.6 MPa at 568°C; FeCl₃ etched, SEM SE-image; slip lines visible inside creep void.

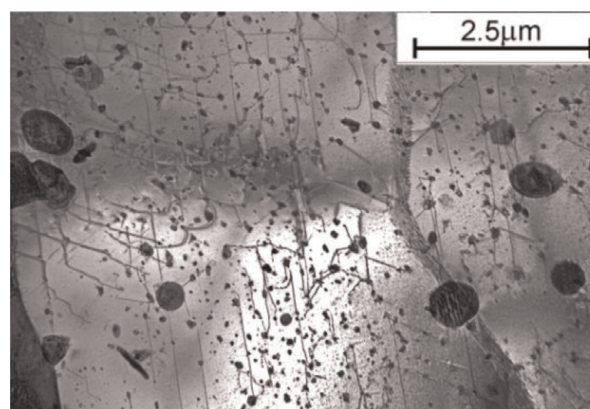**Figure 3.**
½ CrMoV steel crept for 20.5 years at 568°C; precipitates and a/2 <111> dislocations in ferrite; TEM, thin foil ~260 nm thick.
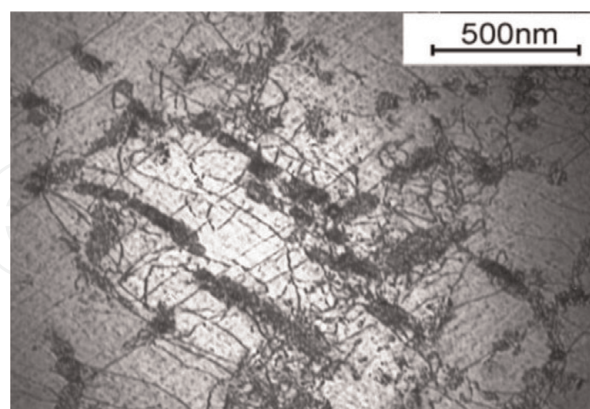

Figure 4.
½ CrMoV steel crept for 20.5 years at 568°C; a/2 <111> dislocations interacting with precipitates; TEM, thin foil ~380 nm thick.

temperature, the voids open up, and on their walls, a characteristic pattern of criss-crossing perpendicular lines can be seen (**Figure 5**) [4]. This evidence confirms the micromechanism of creep microcracks nucleation by piling up mobile dislocations in slip planes at grain boundaries [5] and, after identifying the dislocations and their glide planes, tells that these slip planes are two perpendicular of {110} type. The schematic two-dimensional drawing in **Figure 6** is a model illustrating this situation.

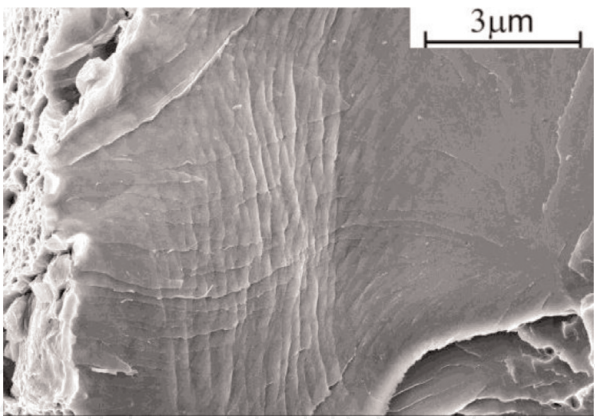**Figure 5.**
Creep crack surface with numerous criss-crossing slip lines, in ½ CrMoV steel exploited for 22.5 years at 568°C; SEM image, no etching.
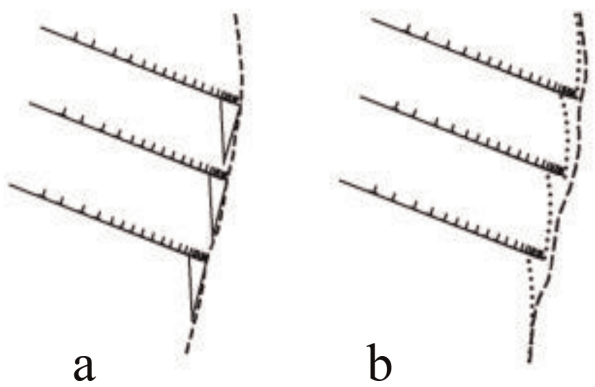

Figure 6.
Schematic drawing of voids (a) and cracks nucleation by the voids coalescence (b) caused by dislocations piled up at grain boundary.
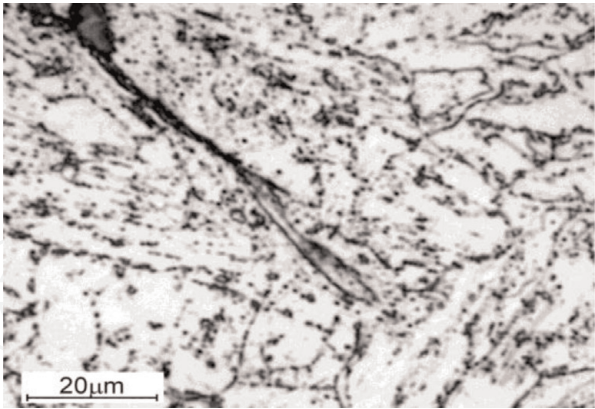

Figure 7.
Microcrack developed near HAZ in P91 steel after service for ~3 years at 568°C; light microscope image, $FeCl_3$ etched.

The $a<001>$ edge dislocations in steel ferrite matrix are known from earlier work as effectively transporting interstitial elements, thus enhancing precipitation rate. During "in-situ" heating experiments in TEM on HSLA steel specimens containing preformed configurations of such dislocations, ultrafine precipitates in fractions of seconds appeared in sites of these dislocations escape and annihilation [6]. In prematurely failed P91 steel higher than average density of fine precipitates appears near to cracks (**Figure 7**). And the generation of substructures containing large amount of such $a<001>$ edge dislocations was observed during deformation of dual-phase steels [7], and also they appeared in this prematurely failed P91 steel (**Figure 8**).
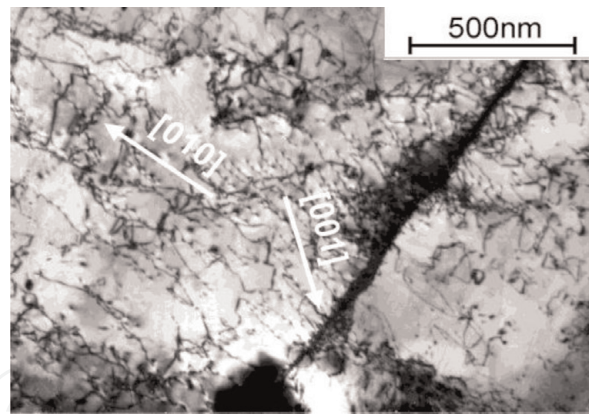
Figure 8.
Substructure of ferrite containing a<001> *edge dislocations in P91 steel after service for ∼3 years at 568°C; TEM, thin foil.*

3. The simulative accelerated creep test

Taking into account the mentioned phenomena associated with creep and implementing the factors speeding up microstructure transformation, the simulative accelerated creep test was designed. It relies on the response of tested material, and for intensifying transformation of microstructure, various programmed testing procedures are used. The ACT was implemented on Gleeble physical simulator using samples with central gauge portion of 12 mm length × 10 mm diameter, mounted like in **Figure 9**. When the span between the "cold" mounting copper jaws is 32–35 mm, the uniformly-heated zone of about 10 mm length is created in the middle of the sample, due to direct resistance heating of the Gleeble balanced by controlled heat flow toward the "cold" Cu jaws. Sizes of the ACT samples are given in **Figure 10**. For testing base steel without weld, plain samples of the same geometry shall be used.

The ACT samples mounted in the Gleeble's "pocket jaws" assembly, like in **Figure 9**, are subjected to programmed cycles of low-cycle thermal-mechanical fatigue, run till failure or till predetermined stress or strain. Loading of the samples is executed by displacement (stroke) control and response of the sample is recorded as force and calculated engineering stress. The ACT procedure uses small elastoplastic tensile and compressive strains applied to central portion of rod-like samples (**Figure 10**) subjected to multiple thermal cycles at temperatures
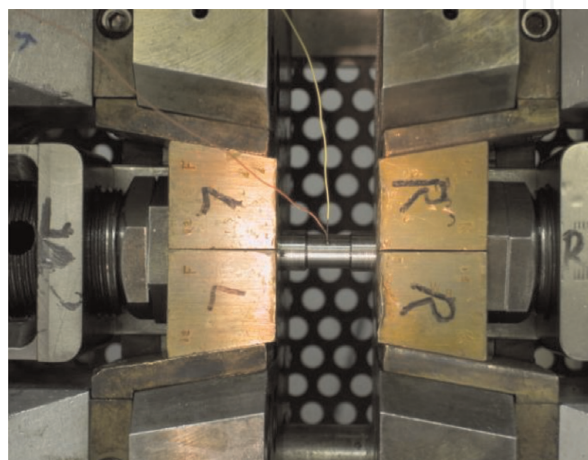

Figure 9.
Mounting of the ACT sample in "cold" Cu-jaws set of Gleeble, with TC percussion welded in the middle of gauge length.
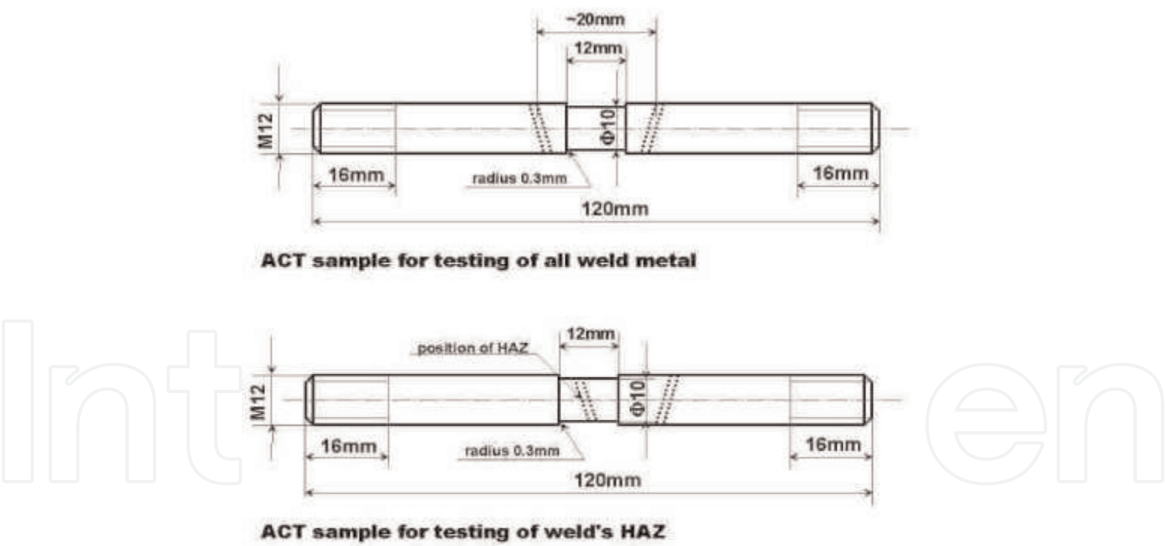
Figure 10.
Schematic drawing of cross-weld samples used for ACT, for testing all-weld-metal and for weld's HAZ.

characteristic of creep. In homogeneous samples, like plain steel bars or all weld metals, often before the crack appearance on the surface, internal cracks are formed perpendicular to the sample's axis. In microstructurally inhomogeneous samples, the cracks follow the "weakest links" like the HAZs of the welds. The ACT speeds up microstructural changes by accumulating elastoplastic tensile and compressive strains in the central portion of the sample during thermal cycling at temperatures characteristic of creep. The compressive strains result in a decrease of yield strength by generation of mobile dislocations, that is, the Bauschinger effect, and this accelerates creep [8]. Then, in the second part of the loading cycle, that is, changing the load to tension, a relaxation time under constant load is applied, during which the sample extends with strain rates equivalent to 10^{-5} to 10^{-8} per second, depending on its stiffness (pseudoelasticity modulus E*) and yield strength.

The shape of the sample's gauge portion after the ACT interrupted before fracturing is given in **Figure 11**. When the heat flow is symmetric to both cold clamping jaws and the tested material is homogeneous, centrally located slight necking forms on the sample often coinciding with an internally nucleated crack (**Figures 11a** and **12a**). **Figure 12b** shows on cross-section of this sample the size of transient zone (TZ) between the grip portion and the uniformly-heated central zone (UHZ). In the case of testing cross-weld sample with weld HAZ, the crack
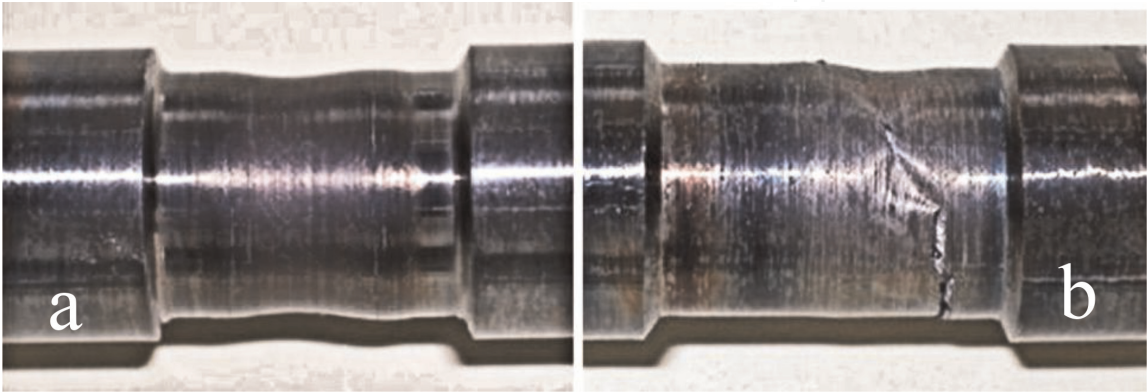

Figure 11.
Shape of the cross-weld, all-weld-metal sample after the ACT terminated before entire fracturing (a), and of weld's HAZ with the crack following the HAZ's direction (b).
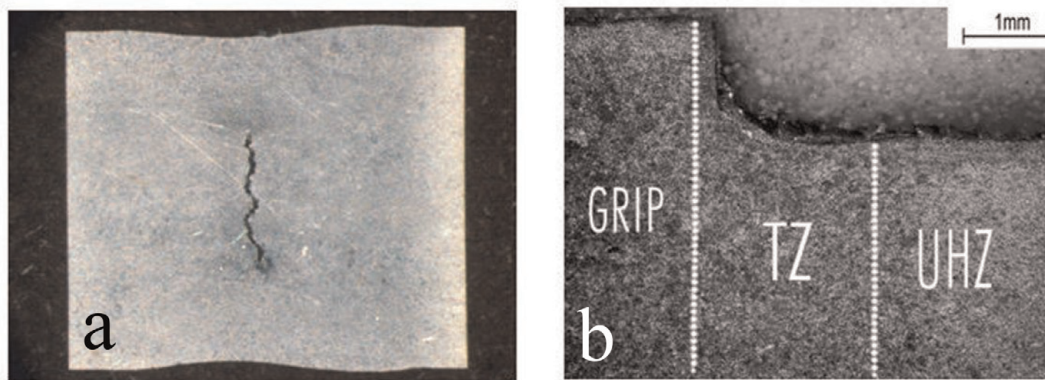
Figure 12.
An internal crack formed in the sample perpendicular to loading axis (a) and size of transient zone between the mounting portion and the gauge portion on the ACT sample (b).

appearing on the surface is often inclined to the longitudinal axis of the sample, following the HAZ (**Figure 11b**).

4. Results of ACT

A characteristic of creep is the decrease of steel hardness with the progress of time. Therefore, any creep test that results in the increase of hardness of sample must be considered as nonreliable. **Table 1** contains examples of initial values for nonexploited materials, for creep exploited materials and for materials subjected to ACT. In the first instance, it shows that during real creep the hardness is most dependent on the time of exposure as well as on the applied stress. Then, the important factor is the initial hardness. Finally, it shows that the drop of hardness after just a few thousand seconds in the ACT follows the tendency of multiyear real creep.

Usually, the tests are run till failure/fracturing, but they can also be stopped anytime and specimens for metallographic, fractographic, and microanalytical investigations can be taken before fracturing. Here, an example is given of the 9Cr-1.5Mo-1.3Co-V-Nb-N-B (FB2) steel, which in as-delivered state has a high-tempered coarse martensitic microstructure (**Figure 13**), while in its as-welded and postweld heat-treated HAZ, such microstructure changes into fine grained, nonacicular with distinguished grains of ferrite. In this pseudo dual-phase micro-structure examined by ACT on crosswise samples, microcracks were found when the ACT was interrupted at about 90% of its duration. Such cracks, as shown in **Figure 14**, were nucleating in intercritically-reheated fine grain portion of heat-affected zone, and they often initiated at specific locations of the HAZ, where two subsequent heat cycles of multipass welding overlapped, giving dual-phase micro-structure.

As the tests for different materials are run at different temperatures and the response of material results in various stresses equivalent to the yield strength at elevated temperature of the test, to compare the ACT results, the duration of the test and its temperature can be included in the following parameter:

$$P_{ACT} = (7 + \log t) \times T/100 \tag{1}$$

where t = time of test in [ks] and T = temperature in [K].

The ACT result can be inserted onto a graph, having P_{ACT} on horizontal axis and average tensile relaxation stress R_S on vertical axis. Alternatively, a creep strength

No.	Material—sample/exposure or test	Hardness HV0.1/(HV30)	
		Initial or (standard)	**After exposure or testing**
1	1/2CrMoV pipe-exp. 22.5 years at 568°C and 16.6 MPa	(180)	(131)
2	1/2CrMoV pipe-exp. 20.5 years at 568°C and 3.8 MPa	(180)	158
3	P91 antler-exp. ~9 years at 600°C and 16.5 MPa	(250)	229
4	P91 weld-exp. ~9 years at 600°C and 16.5 MPa	(265)	208
5	P91 rolled pipe-exp. ~3 years at 568°C	(250)	231
6	P91 weld with PWHT-exp. ~3 years at 568°C	(265)	258
7	P91 forged bottle-exp. ~3 years at 568°C	(260)	243
8	12Cr1MoV-exp. 16 years, 550°C, 15 MPa + ACT 600°C, 19.5 ks	188	164
9	15Cr1Mo1V-exp. 18 years, 550°C, 15 MPa + ACT 600°C, 30.4 ks	176	157
10	P22 rolled pipe + PWHT/ACT 600°C, 9.5 ks	234	188
11	P22 weld metal + PWHT/ACT 600°C, 11.3 ks	238	202
12	P22 rolled pipe HAZ + PWHT/ACT 600°C, 6.4 ks	227	196
13	P91-std. weld with PWHT/ACT 600°C, 28.3 ks	287	230
14	P91-std. weld with PWHT/ACT 600°C, 82.6 ks	285	223
15	P91-std. weld with PWHT/ACT 625°C, 37.6 ks	285	217
16	P91-temper-bead weld, no PWHT/ACT 620°C, 51.3 ks	298	193
17	P92-std. weld with PWHT/ACT 625°C, 21.3 ks	294	240
18	P92-rolled pipe HAZ/ACT 625°C, 22.1 ks	268	228

Table 1.
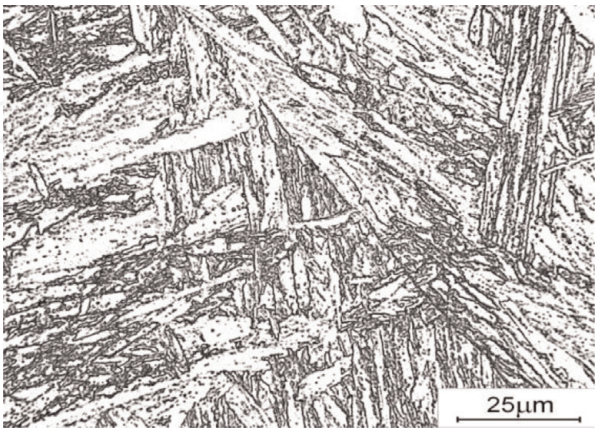*Examples of hardness for steels subjected to creep and/or ACTested.*

Figure 13.
High-tempered martensite of forged 9Cr-1.5Mo-1.3Co-V-Nb-N-B (FB2) steel in as-delivered state, FeCl₃ etched.

factor in ACT can be given as: $F_{ACT} = P_{ACT} \times R_S/100$ and used for comparing materials tested at the same conditions.

During the ACT procedure, the data of stress, strain, strain rate, and temperature, as well as dilatometric information, can be recorded, out of which strain-time and stress-time graphs are produced as shown in **Figures 15** and **16**.
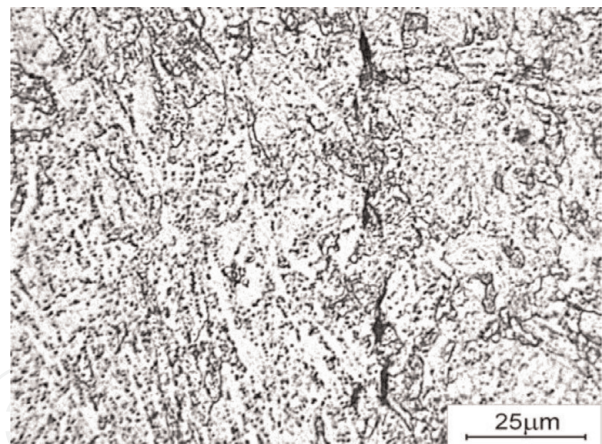
Figure 14.
Microcracks in IC-HAZ of FB2 steel perpendicular to load axis of ACT sample, developed at ~85% of test duration at 625°C.
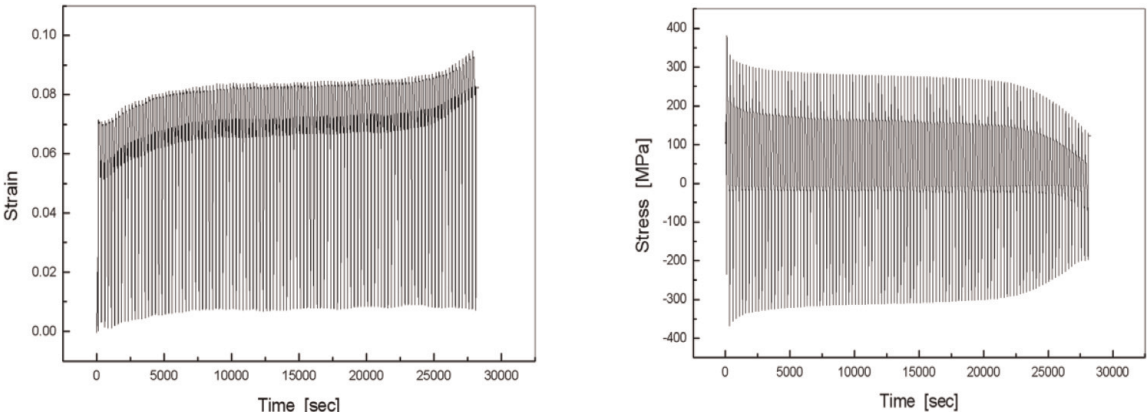

Figure 15.
Typical strain-time and stress-time graphs from ACT on a "soft" alloy, for example, postweld heat-treated P91 weld metal.
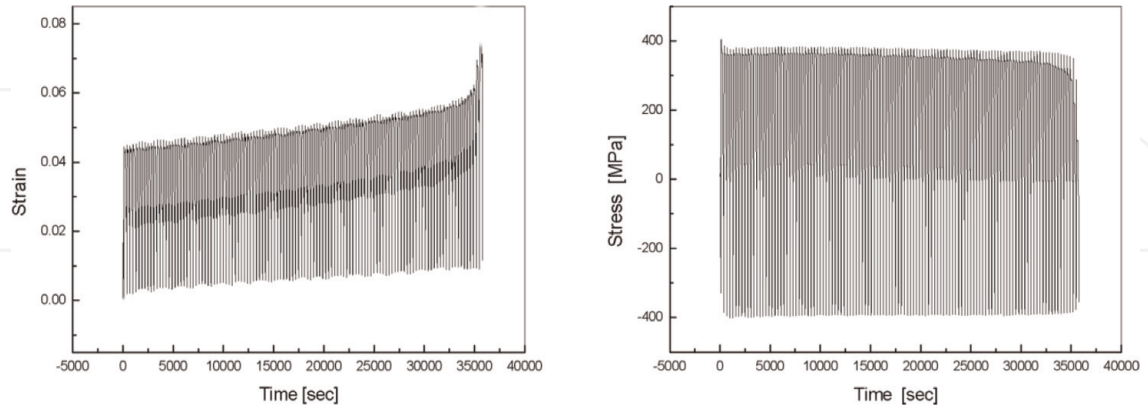

Figure 16.
Typical strain-time and stress-time graphs from ACT on a "hard" alloy, for example, as-deposited (without PWHT) P91 weld metal.

The results of ACT are usually plotted in the form of strain-time and stress-time graphs, and data from these graphs are used to calculate creep strength and true creep life. The "zero-stress" line on strain-time graph from ACT well resembles the true creep graph from conventional creep tests.

Examples of results obtained at different ACT temperatures for various P91 weld metals in as-welded state (AW) and postweld heat treated (HT) are given in **Table 2**.

The result of P91-HT2 is complimentary to sample #16 from **Table 1**, to which after temper bead welding the PWHT was applied for 2 h at 720°C in furnace, and then the ACT was run. Longer durations of some tests (P91-HT2 and P91-HT5) resulted from smaller loading displacements applied in such lower intensity ACT program. The tests are usually run at prevacuum of about 10^{-3} Tr maintained in the testing chamber of physical simulator; however, when clean fracture surfaces are expected after the ACT, high vacuum of better than 10^{-5} Tr may be applied. In these experiments on P91 steel, no difference in test duration due to vacuum level was observed. Visible difference in test duration was noted when water mist became introduced into the testing chamber; the result of P91-HT5m in **Table 2** shows shorter test duration, lower tensile relaxation stress, and in consequence lower creep strength factor. On cylindrical surface of this sample's gauge portion, numerous fine cracks appeared (**Figure 17**), which for the sample tested in high vacuum could not be seen up to the macrocrack appearance on the surface (**Figure 18**).

To verify the results of ACT by proving that the test adequately simulates situations appearing in real creep, metallographic investigations were carried out. **Figure 19** shows dislocation substructure of P91 weld metal at half-life of the ACT. In recovered postmartensitic subgrains criss-crossing, $a/2$ <111> screw dislocations appear in vast amount and form planar arrays.

Material and state	ACT temp. [°C]	ACT time to fracture [ks]	Tensile relaxation stress R_S [MPa]	Creep strength factor F_{ACT} [MPa]
P91-AW1	625	22.0	305	228
P91-HT1	625	37.6	273	210
P91-AW2	620	38.0	395	303
P91-HT2	620	51.3	177	138
P91-HT3	600	28.3	325	240
P91-HT4	600	26.3	318	233
P91-HT5	600	82.6	336	262
P91-HT5m	600	57.2	266	203

Table 2.
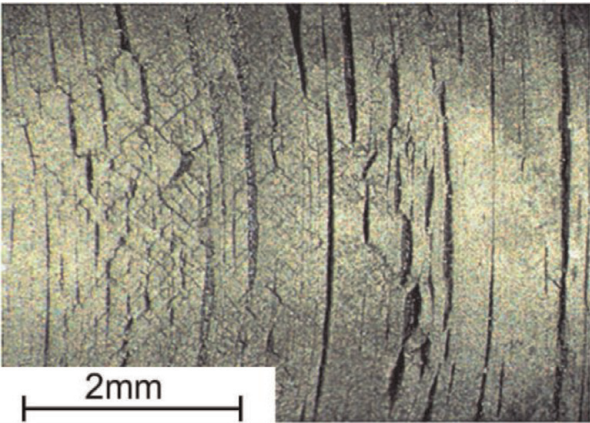*Examples of ACT results.*

Figure 17.
Cylindrical surface of gauge portion on P91 ACT sample after test at 600°C with the presence of water mist in working chamber.
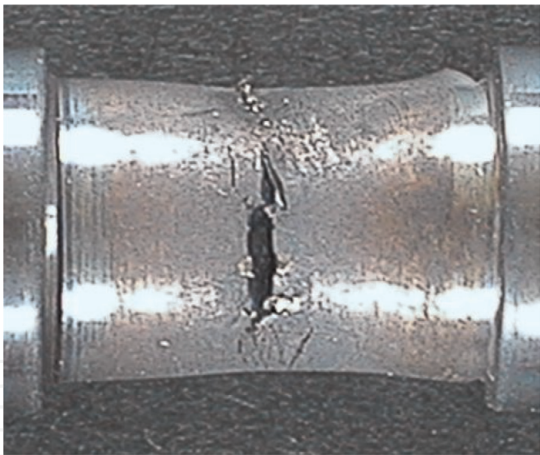
Figure 18.
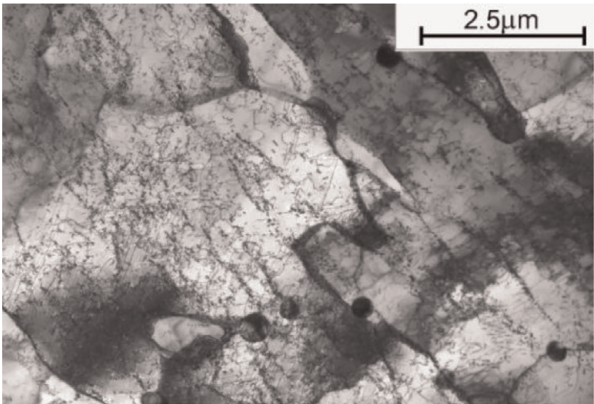*Macrocrack on ACT sample tested at 600°C with high vacuum in simulator's working chamber.*

Figure 19.
Subgrains with recovered dislocation configurations at half-life in ACT, in P91 weld metal sample tested at 600°C; TEM, thin foil.
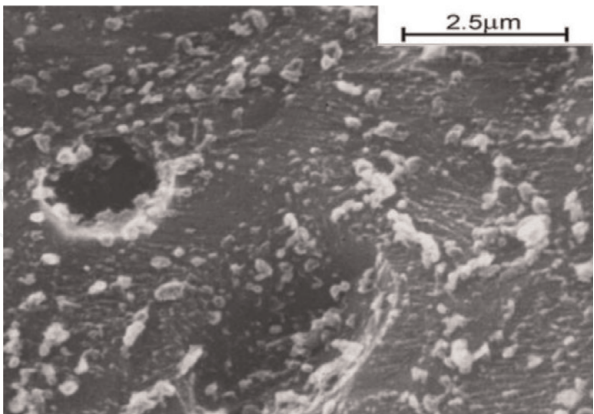

Figure 20.
Fracture surface of ACT sample of P91 steel showing high density of carbides, electro-polished and FeCl₃ etched, SEM image.

In **Figure 20**, the fracture surface of ACT sample is shown, after the removal of surface oxides by electropolishing and then etching. On this surface, the traces of slip lines can be recognized, thus confirming the fracture nucleation by slip and piling up dislocations in planar arrays.

The final verification has to be done on TEM images of the tested steel or weld metal before and after the ACT, like on the examples presented here in
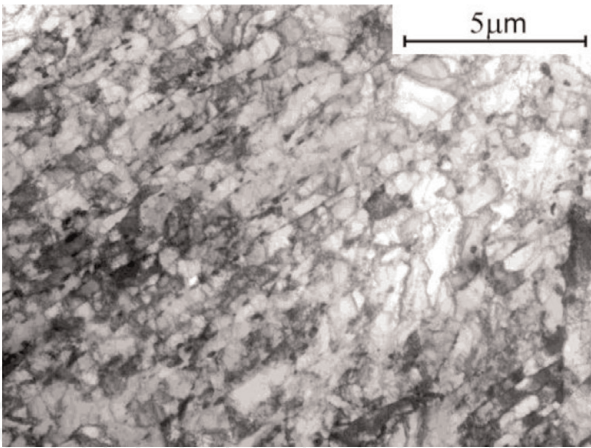
Figure 21.
Arrays of subgrains with carbides in the initial microstructure of P91 weld metal before the ACT; TEM, thin foil.
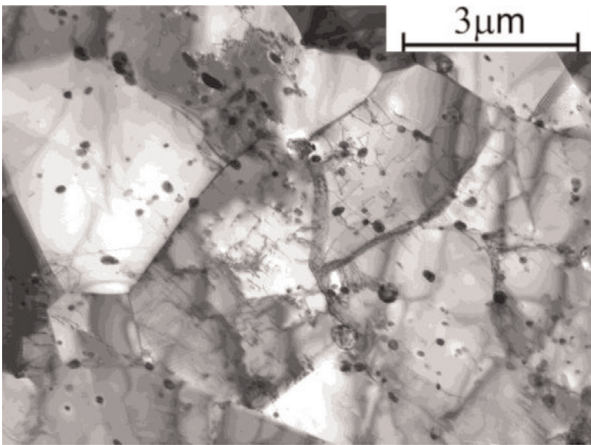

Figure 22.
Well-recrystallized ferrite grains with arrays of carbides, in P91 weld metal sample after completed ACT at 600°C; TEM, thin foil.

Figures 21 and **22**. These figures show the microstructure transformation in P91 weld metal from tempered lath martensite before the ACT to fully recrystallized after the ACT equiaxed ferrite grains with coagulated and spheroidized carbides, the last aligned in directions following prior martensite laths.

5. Combination of weld's HAZ simulation with ACT

The ACT procedure appeared useful to study other high strength steels for elevated temperature applications different than thermal power generation and chemical processing.

Table 3 contains results of ACT on nuclear reactor pressure vessel steel grade 15Ch2MFA (Russian), of which creep resistance is not the most important property; however, the strength of its HAZ after welding and PWHT is crucial. Physically-simulated HAZs on this steel were earlier studied and reported, as regards their microstructures and CVN impact strength [9]. The initial microstructure of 15Ch2MFA steel was high-tempered martensitic (**Figure 23**), and after the single-cycle 900°C physical simulation of HAZ, it changed into a ferritic-martensitic mixture in the middle of the simulated HAZ (**Figure 24**), with well-distinguished equiaxed fine bright ferrite grains and darker-etching areas, details of which could not be revealed by light microscopy.

	Material	ACT temperature [°C]	Time to fracture [ks]	Average tensile stress [MPa]	Creep life for 100 MPa [h]
1	Base 15Ch2MF steel	625	10.18	203	4183
2	15Ch2MF, HAZ 1-cycle simulated, no PWHT	625	8.81	235	2810
3	15Ch2MF, HAZ 1-cycle simulated + PWHT	625	12.37	187	5547
4	15Ch2MF, HAZ 2-cycle simulated + PWHT	625	8.12	264	9765
5	15Ch2MF, HAZ* 2-cycle simulated + PWHT	625	10.66	183	5873

Table 3.
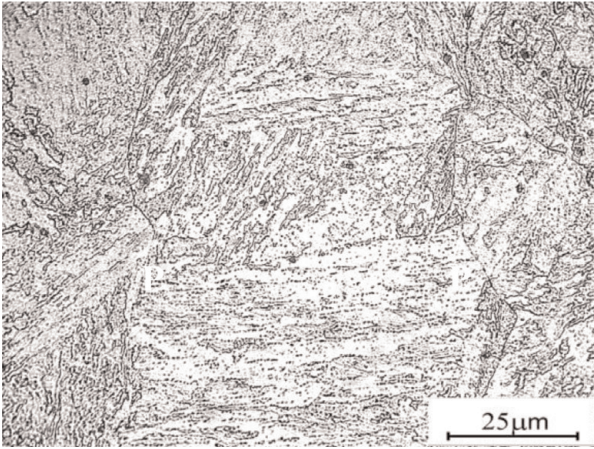*Creep life of simulated HAZs in 15Ch2MFA steel.*

Figure 23.
Initial high-tempered martensitic microstructure of 15Ch2MFA steel.
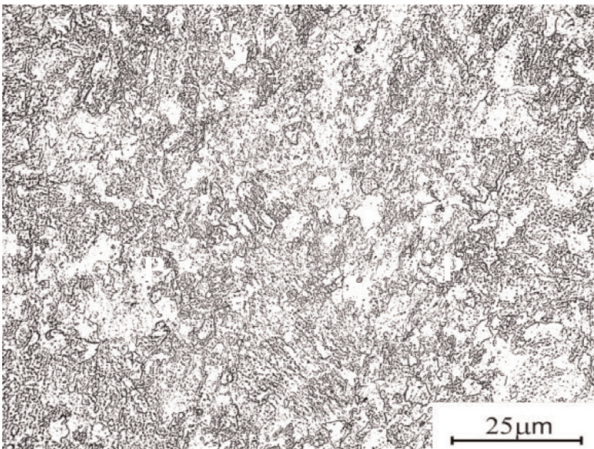

Figure 24.
Simulated intercritically-reheated microstructure of 15Ch2MFA steel HAZ.

More informative as regards components of this intercritical HAZ are TEM images from thin foil specimens, which reveal small compact martensitic islands with nondissolved carbides in the HAZ region representative to temperatures just above the A1 (**Figure 25**) and larger fields of homogeneous acicular martensite surrounded by ferrite grains (**Figure 26**) in the region closer to the 900°C peak
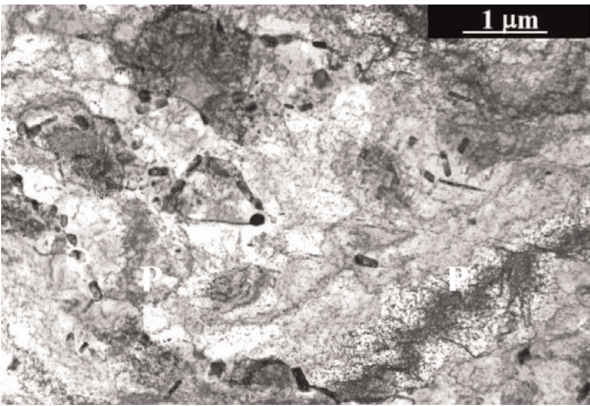
Figure 25.
Ferritic-martensitic microstructure with retained carbides in simulated HAZ region close to A1 (760°C) temperature.
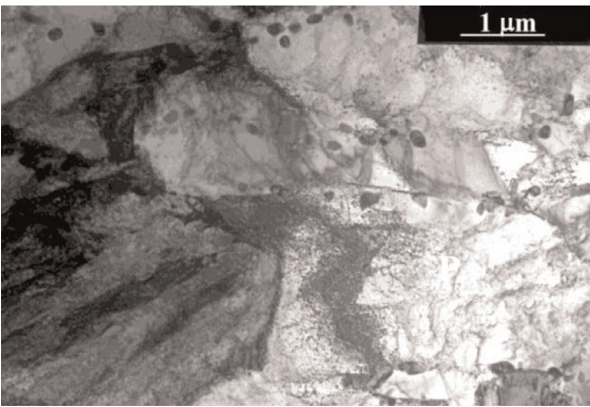

Figure 26.
Martensite grain and recrystallized ferrite, in simulated HAZ region close to peak (900°C) temperature.

temperature of the simulation cycle. In both cases, the ferrite interacting with martensite contained very high dislocation density. More details of this microstructure in as-simulated state and after conventional tempering were given in previous IIW-Document [9].

Creep life of the weld's simulated HAZ on this steel was tested using the simulated welding thermal cycle(s) followed immediately by ACT, applying setups as shown in **Figures 27** and **28**. Various simulations of the welding thermal cycles were carried out and then, by manipulation of the stress intensity in ACT, the
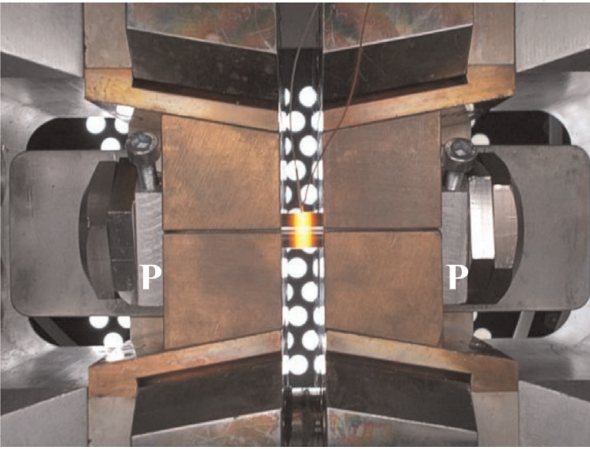

Figure 27.
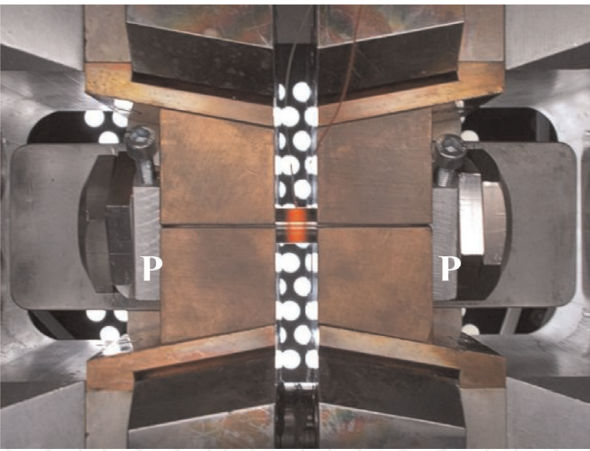*The ACT sample in Gleeble chamber during simulation of HAZ's 1st cycle.*

Figure 28.
The same sample in Gleeble chamber during simulation of HAZ's 2nd cycle.

strain-induced precipitation was achieved revealing potential of this steel to strengthen in the HAZ. However, not only the stress intensity but also the locations of post dual-phase microstructure generated by subsequent weld thermal cycles, that is, the second cycle of 920°C peak after the first cycle of 1220°C peak, contributed to the exceptionally high creep life of the HAZ in the case of sample #4 (result in row 4 of **Table 3**). In classical welding HAZ simulation experiments, the thermal cycles are executed having their peak temperatures in the same locations on the fixed sample (see **Figures 27** and **28**), and in consequence, the intercritically reheated zone of the second cycle does not overlap with the similar zone from the first cycle, as it appears closer to the peak temperature location than in the first cycle (**Figure 29**) [10], while in many true multibead welds, these overlap zones are vulnerable to initiation of voids and cracks, in particular during creep. Result #4 from **Table 3** shows an exceptionally high value due to the overlap of the intercritically reheated HAZ portion of the second simulation cycle (peak 920°C) with the fine martensitic microstructure of the previous simulation cycle (peak 1220°C).

The intercritically reheated zones after a single-cycle simulation at 1220°C appear at about 1.0–1.5 mm closer to the cold Cu jaws, than at the simulation with the peak temperature at 920°C, with the same span between the Cu jaws. To correct this difference, distance plates (P) can be used in the clamping assembly of the Gleeble, and the first thermal cycle, for example, 1220°C, was being executed with both plates inside, while for the second cycle, for example, 920°C peak, one of the plates is removed, and this type of simulation was marked HAZ*. It allowed intercritical zones from both cycles to overlap and resulting microstructures of HAZ* did not differ from those of real welds. To carry out the ACT after the HAZ* cycle simulation, both distance plates have to be removed and thus the free span
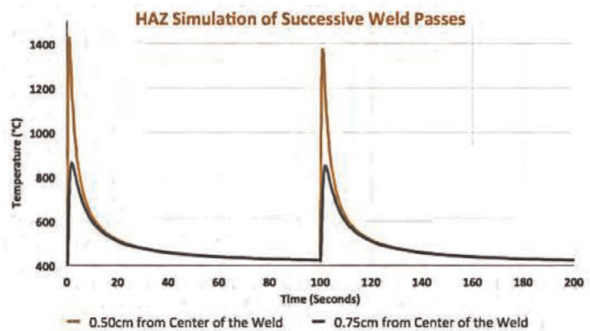

Figure 29.
Thermal graph of two-cycle HAZ simulation on Gleeble [9].

15

between jaws increased, to secure the uniformly heated hot working zone of about 10 mm length on the ACT sample, as shown in **Figure 30**. The test depicted on this figure was carried out in a low vacuum of the working chamber, so the "hot" portion of the ACT sample visibly oxidized.

The last row (#5) in **Table 3** shows the creep life of two-cycle HAZ*-simulated sample after ACT carried out at lower stress intensity, and the fracture on this sample appeared eccentrically close to the location in which both intercritically reheated zones overlapped. Thin foils for TEM observations taken as close as
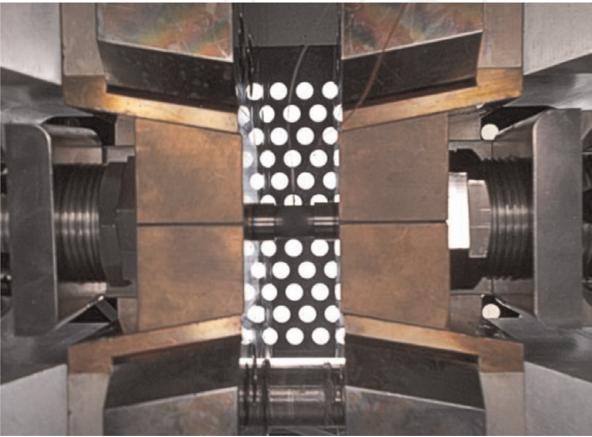

Figure 30.
The HAZ-simulated sample in Gleeble chamber during the ACT, before cracking.
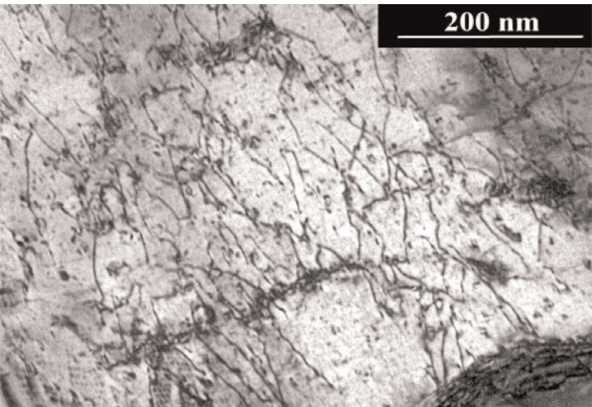

Figure 31.
High density of ultrafine precipitates in ferrite in the two-cycle 1220°C/920°C HAZ-simulated sample (4) with PWHT, after ACT of high stress intensity; foil thickness ∼360 nm.
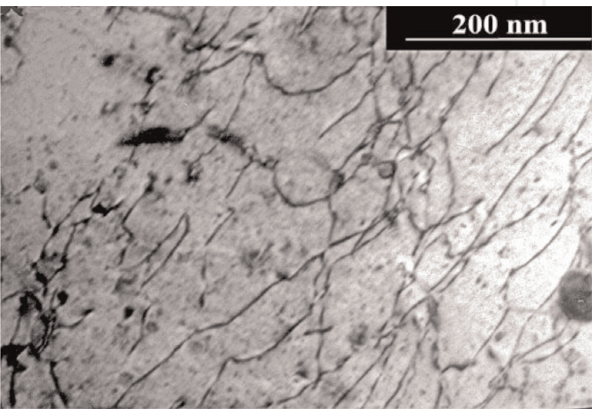

Figure 32.
Dislocations with fine precipitates in ferrite in a single-cycle 1220°C HAZ-simulated sample (3) with PWHT, after ACT of normal stress intensity; foil thickness ∼450 nm.

possible (i.e., ~0.3 mm) to the fractures of samples (#4) and (#5) revealed substantial differences of ferrite substructures of the 15Ch2MFA steel HAZs, as to the dislocation density and dispersion of ultrafine precipitates (**Figures 31** and **32**). This strengthening of simulated weld HAZ in the 15Ch2MFA steel as well as increase of its creep life can be related to the strain-induced precipitation forced by multicycle intensive loading during ACT.

6. Evaluation of creep life from ACT data

The up-to-date ACT procedure includes evaluation of true creep life. Out of the collected test's rough data, the stiffness of material, that is, pseudoelasticity modulus E^* and then the creep life, can be calculated for a nominal stress, for example, 100 MPa. Some examples from recent research [11], on forged FB2 steel (9Cr-1.5Mo-1.3Co-V-Nb-N-B) and a weld on it, are given in **Table 4** in rows 1–4. In this research, one of the main questions was how much the HAZ on samples taken from real welds has been weaker than the base material, and ACT combined with the HAZ simulation allowed to answer this.

The FB2 grade belongs to the family of new creep resisting steels, developed and tested in EU R&D COST-522 and COST-536 collaborations. In these COSTs, also conventional creep tests were carried out, and for comparison, some of their results are given in **Figure 33**. The result creep life in ACT at 650°C on FB2 steel, that is, 8656 h, matches quite well with the upper black line of the graph presented.

An additional question was if by physical simulation of welding thermal cycles, similar creep properties of HAZ can be obtained and the answer was not straightforward. Physical simulation of two HAZ thermal cycles "one on another," with the first peak temperature of 1220°C followed by the second one of 920°C peak and PWHT "in situ" at 720°C for 15 min, gave in ACT an optimistic result of almost 25,000 h at nominal stress of 100 MPa and temperature of 625°C. The application of the modified HAZ* simulation procedure, mentioned before for the 15Ch2MFA steel, gave after ACT a result similar to creep life of HAZs in real FB2 welds, and the result of this modified HAZ* simulation followed by ACT is included in row 6 of **Table 4**.

The ACT samples for this research were taken from the FB2 material used for the preparation of dissimilar weld joint from forgings of two rings (external diameter 600 mm and thickness 200 mm) made of steel types COST FB 2 and COST F [13]. The heat treatment after the forging of FB2 was 1070°C/6.5 h + 570°C/12.5 h + 710°C/24 h. The weld was manufactured by automated TIG hot wire method in a narrow gap with internal protection by argon, using filler material PSM

	Material	ACT temperature [°C]	Time to fracture [ks]	Average tensile stress [MPa]	Creep life for 100 MPa [h]
1	FB2 base	675	18.04	134	4156
2	FB2 base	650	19.99	149	8656
3	FB2 base	625	9.89	144	27,169
4	FB2 HAZ	625	8.11	196	16,670
5	FB2 HAZ	625	10.59	182	18,636
6	FB2 sim HAZ*	625	9.64	192	17,423

Table 4.
Creep life calculated from ACT data.

Thermanit MTS 616. The thickness of the weld was 120 mm. The chemical compositions of the base material FB2 and the filler metal are given in **Table 5**.

From these welds, smooth cross-weld specimens were fabricated for long-term conventional creep tests (CCT), which were carried out in air at temperatures ranging from 550 to 650°C at stresses from 70 to 220 MPa. Samples from the same weldment were subjected to ACT in order to simulate structure transformations after long-term CCT. ACT was executed at VSB-Technical University Ostrava (Czech Republic) on an HDS-20 physical simulator and partly in the laboratory of the simulator manufacturer (DSI). ACT temperatures ranged from 575 to 650°C (**Figure 33**).

In its initial, as-delivered state, the steel has a high-tempered martensite microstructure, as given in **Figure 13**. This microstructure, as seen on TEM images, shows tempered former martensite laths, retaining high density of dislocations and having chains of particles precipitated along the lath boundaries (**Figure 34**). Most of the precipitates along the former lath boundaries were identified as carbides, while some of the larger-than-average ones appeared to be Laves phase Fe_2Mo. In postmartensitic laths and in elongated ferrite grains, numerous recovery-type planar configurations of criss-crossing dislocations can be observed at larger magnifications (**Figure 35**).

The initial microstructure of the FB2-BM, as seen in light microscope (LM), is highly-tempered martensite of acicular morphology (**Figure 36**). In the as-welded HAZ, it is changed into a very fine-grained one, hard to resolve by light microscopy (**Figure 37**).

Details of the HAZ microstructure are revealed on the following TEM pictures taken from thin foil specimens. As the HAZ is expected to be the weakest part of the weld and consequently of the ACT sample, to take the specimens for TEM observations from exact HAZ location just before their fracturing, the tests had to be run

Material	Element content in wt.pct												
	C	Mn	Si	Cr	Ni	Mo	V	Co	W	Nb	N	B	Al
FB2 steel	0.13	0.34	0.05	9.60	0.17	1.48	0.20	1.32	—	0.059	0.016	0.0079	0.007
MTS 616	0.11	0.32	0.30	8.87	0.57	0.56	0.18	0.15	1.49	0.051	0.018	0.0036	0.009

Table 5.
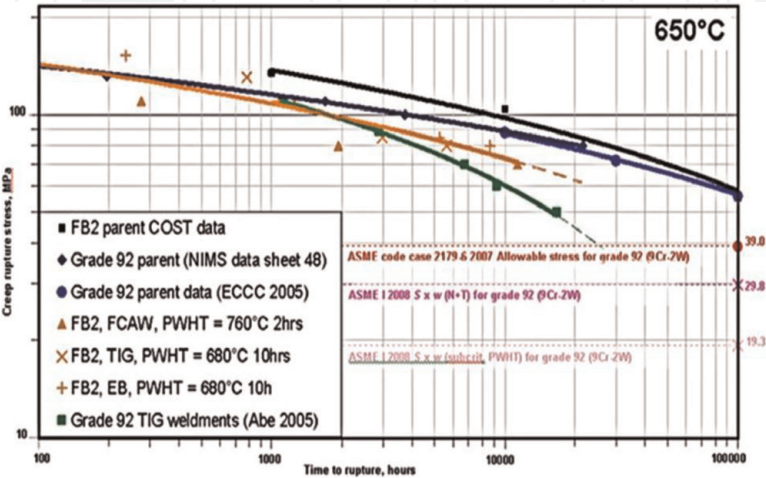*Chemical compositions of FB2 and weld metal.*

Figure 33.
Creep rupture plot showing the performance of FB2 parent material and weldments, relative to grade 92 (9Cr-2W) seamless pipe [12].
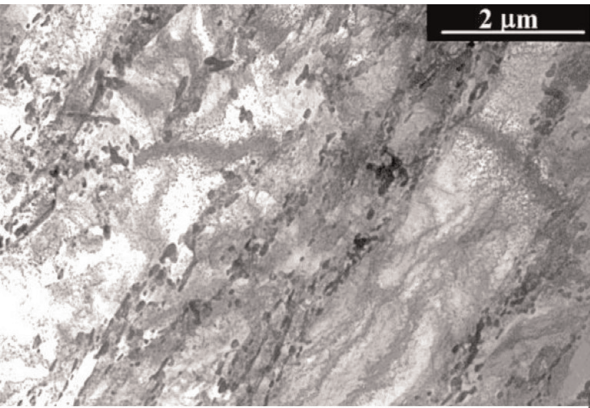
Figure 34.
High-tempered lath martensite microstructure of FB2 steel in as-delivered, i.e., forged and stress-relieved (AD), state.
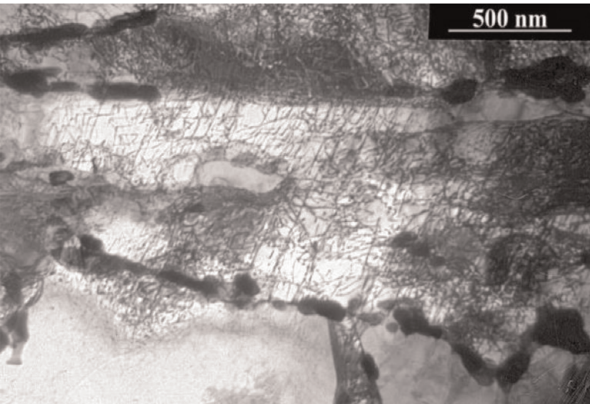

Figure 35.
Criss-crossing dislocation arrays in high-tempered lath martensite in FB2-AD steel with carbides along former lath border.

Figure 36.
FB2-BM microstructure in as-delivered state, before ACT, LM.

till 85–95% of the expected time to fracture. Therefore, in the ACT program, a force limiting stop was placed in the tensile relaxation portion of the testing cycle. Typical force-time graph of ACT on plain FB2 steel (sample FB22) is given in **Figure 38**, showing how the initial tensile relaxation force of ∼2200 kgf decreases to ∼1400 kgf at 90% of the test duration.

In the initial, as-welded microstructure of HAZ, in its under-critical portion at A1 temperature, the lath martensite recrystallizes, while near to colonies of carbides, first traces of austenite form. Some ferrites get the shape of large laths (**Figure 39**), while in other ferrite grains next to austenite with carbides, very high
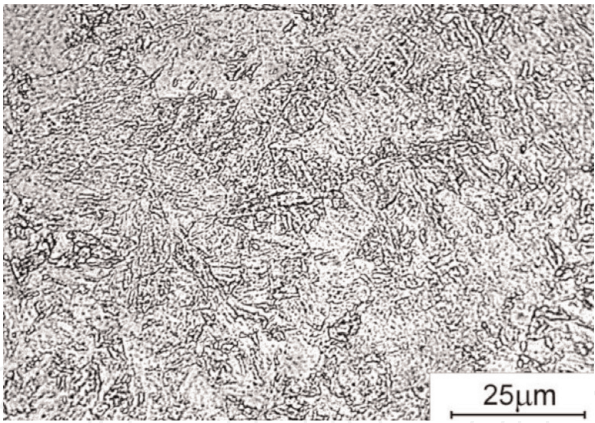
Figure 37.
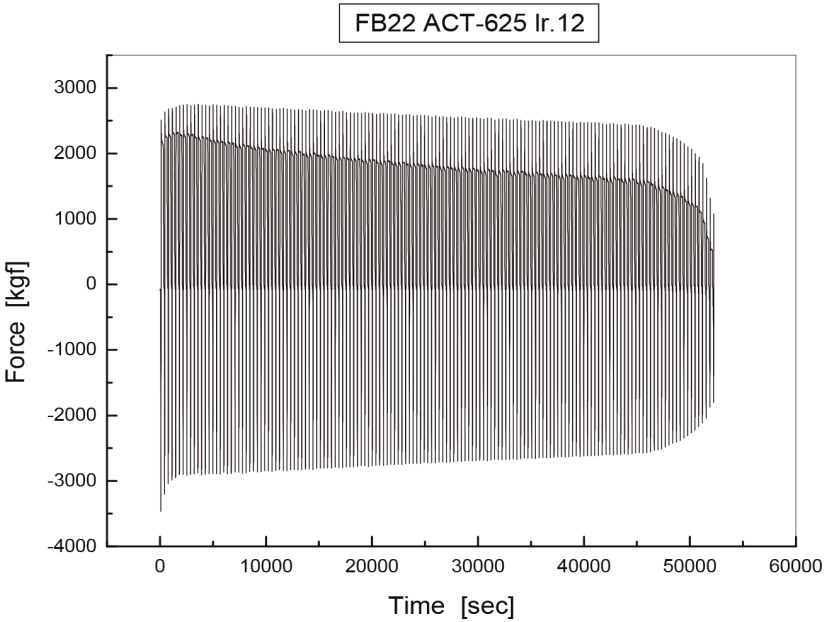*FB2 weld's HAZ microstructure in as-delivered state, before ACT, LM.*

Figure 38.
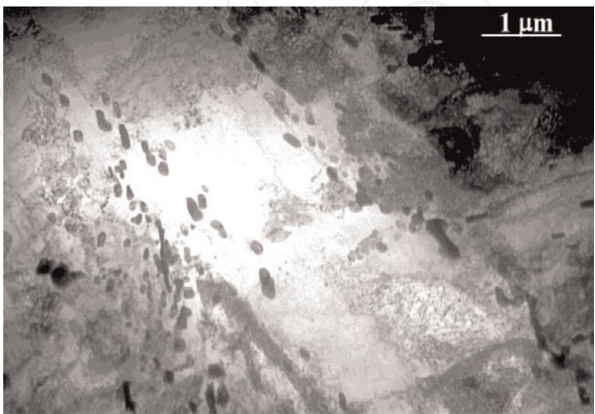*Typical force-time graph from ACT on FB2 steel.*

Figure 39.
Large ferrite lath in as-welded FB2 HAZ at location near to A1 temperature.

dislocation density is generated (**Figure 40**). In intercritical portion of HAZ, the austenite forms more compact islands, while some of the carbides still remain undissolved. Finally, above the A3 temperature, austenite becomes more fine-grained homogeneous and close to the fusion surface with the weld metal
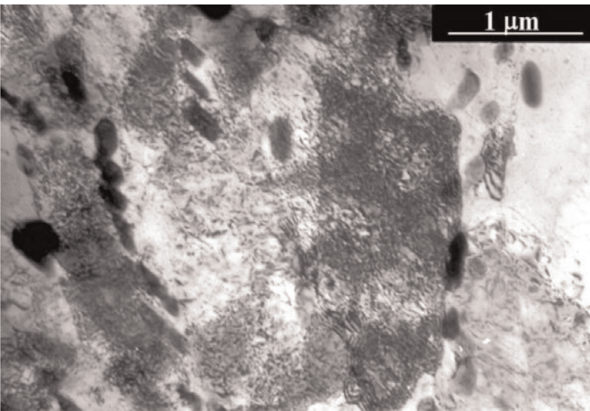
Figure 40.
High dislocation density between nondissolved carbides in as-welded FB2 HAZ microstructure of FB2 in as-delivered state, before ACT, TEM 15,000×.
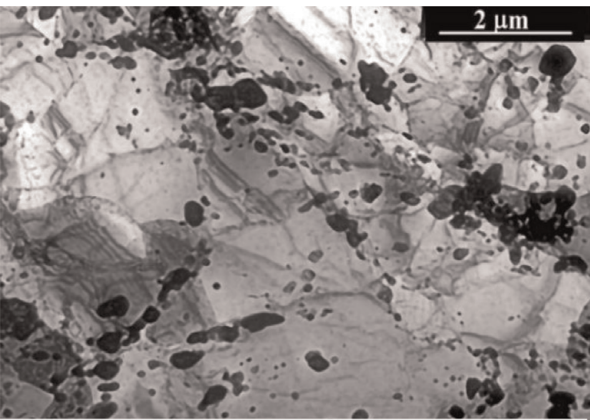

Figure 41.
IC-HAZ in FB2 with recrystallized ferrite and precipitates, after ACT at 625°C.
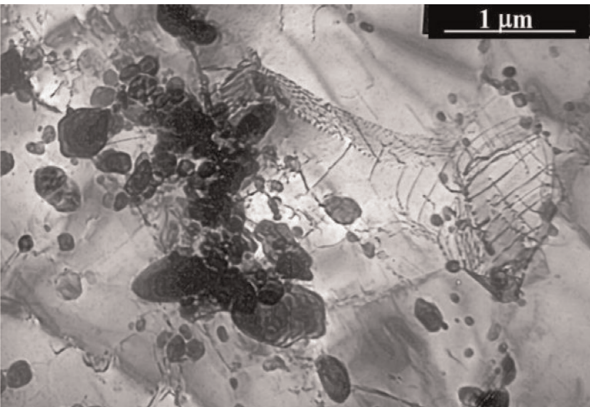

Figure 42.
Agglomerates of precipitates in FB2 weld IC-HAZ after ACT at 625°C.

coarse-grained, which transforms to acicular martensite on cooling. To take the TEM thin foil specimens from the HAZs on ACT samples, from the first tested cross-weld sample, the time to fracture was learned and the force stop equivalent to 90% of this was placed in the program. Applying ACT to the as-welded HAZ microstructures forces their high tempering with very intensive precipitation of carbides. The ferrite in the intercritical portion of HAZ, which contains very few carbides, recrystallizes generating equiaxed grains, while along this ferrite, dense bands with agglomerates of carbides are formed (**Figure 41**). Some largest precipitates in these bands look like undissolved carbides from the initial HAZ
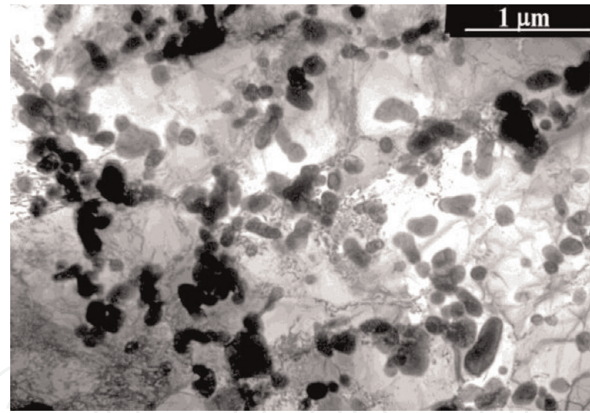
Figure 43.
Carbides in FB2 HAZ at location above A3 temperature, ACT at 625°C.
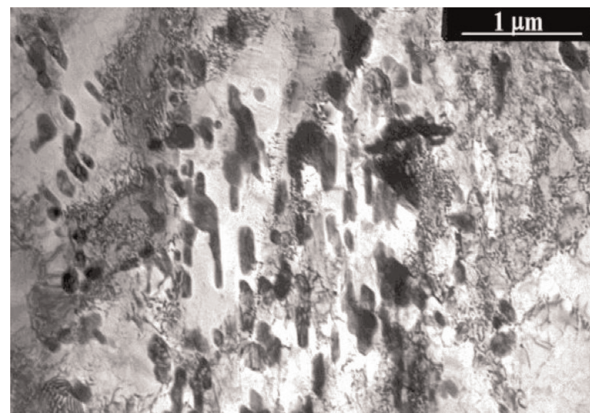

Figure 44.
Carbides in FB2 HAZ at location near to fusion line, ACT at 625°C.

microstructure, while numerous finer ones should be considered as of tempering type (**Figure 42**).

In the HAZ portion representing above A3 temperature, that is, of mainly austenitic as-welded microstructure, high density of partly spheroidized carbides appear and the largest precipitates seldom appear (**Figure 43**), while in the HAZ portion near to the fusion surface, the carbides in high-density colonies are partly elongated and aligned in the directions of former martensite laths (**Figure 44**); here, some larger precipitates do appear again.

ACT executed on the weld HAZ and interrupted before fracturing of sample allows taking proper specimens for TEM observations, which in turn show clearly how the separation of phases, ferrite and austenite, in the intercritical region produces during creep the microstructure vulnerable to premature failure.

7. Discussion

The simulative accelerated creep test was developed for martensitic-ferritic creep resisting steels and welds, based on detailed substructure observations of crept steels. Dislocation configurations governing the real creep were reproduced in a low-cycle compression-tension multicycle procedure carried out at the testing temperatures similar to those of real creep. This procedure applied on Gleeble physical simulator caused in less than 12 h transformation of the initial tempered martensite substructure into fully recrystallized ferrite with spheroidal or coagulated carbides and adequate decrease of hardness similar to that after multiyear

exposure to real creep. The carbides and Laves phase precipitates, after ACT, did not reach sizes of these after real creep, but their amount and density appeared substantially larger. The more intensive nucleation of precipitates has been characteristic of electro-thermal treatment [14] and this way the direct resistance heating in Gleeble [1] plays a role in acceleration of the process. The larger density of precipitates, despite their smaller sizes, results in a similar or even more substantial depletion of matrix in alloying elements like in the long-term real creep. The strains applied in each cycle of the ACT procedure are too small to homogenously deform the tested material in any of the individual cycles to cause dynamic recovery or recrystallization. The dislocation configurations generated in each deformation cycle accumulate from cycle to cycle mainly in the preferentially oriented components of microstructure and after reaching critical density annihilate, gradually contributing to generation of voids and cracks, simulating the real creep in this way. Finally, on the crack surfaces after ACT, very large amounts of precipitates are present and also characteristic lines of dislocation escape appear. As to the chemical compositions of precipitates after ACT, in an earlier study on P91 steel [15], the microanalysis results from precipitates after ACT matched those of the crept steels and complied with ThermoCalc equilibrium predictions.

Up to now, the ACT procedure was applied in a study on development of P24 grade welding consumables [16] and new steels for supercritical components of power generation systems [17], as well as for determining remnant life of crept steels and repair welds [18]. Finally, in combination with weld thermal cycle simulation, it offered an opportunity of fast optimization for welding procedures to address problems of weakening heat-affected zones of welds.

The ACT procedure does not force the material to fail by overloading. By cyclic compressing and stretching of the tested material, ACT records response of the material while choosing the most prone sites in microstructure for nucleation of voids and cracks, thus well simulating the real creep. Programmed various amounts of compressive and tensile strains in combination with thermal cycles affect the intensity and duration of test as well as promote precipitation, making in intended manner the ACT plausible for study of creep-fatigue situations, importance of the last has been growing recently due to possible instability of grid by incorporating various energy sources. The conventional standard long-term creep tests cannot address this last issue.

8. Conclusions

1. Low-cycle thermal-mechanical fatigue of martensitic-ferritic creep resisting steels, applying direct electric resistance heating, accelerates transformation of microstructure and intensifies precipitation of secondary phases, causing depletion of matrix in alloying elements similar to that occurring during the real creep.

2. A substantial role in the accelerated microstructure transformation is played by meta-stable $a<001>$ edge dislocations, which effectively transport interstitials, thus accelerating precipitation.

3. From the accelerated creep tests as well as from conventional case studies appears that the applied stresses and accumulated strains speed-up weakening of the matrix and promote local failures in the most vulnerable sites of microstructure.

4. Hardness measured at room temperature after ACT indicates the extent of microstructure transformation; however, when the material will fail cannot be predicted.

5. Calculation of true creep life from ACT is possible, taking into account changing of stiffness of material at the elevated temperature of the test, its flow stress, and duration of the test.

6. A combination of the weld's HAZ physical simulation with the direct execution of ACT allows speeding up the development of optimum welding technology.

7. In general, within the relatively short time of the ACT's duration, large amount of data can be generated, which are needed for the development of improved new materials and technologies.

8. The simulative accelerated creep test can be a useful alternative to the existing standardized long-term tests especially that it is giving adequate transformation of microstructure in much shorter time than the conventional tests and can also provide materials data relevant to creep-fatigue situations.

Author details

Stan T. Mandziej
Advanced Materials Analysis, Enschede, The Netherlands

*Address all correspondence to: stanamanl@cs.com

IntechOpen

References

[1] Available from: www.gleeble.com/products.html

[2] Honeycombe RWK. Creep in pure metals and alloys. In: The Plastic Deformation of Metals. London: E. Arnold Publishers; 1984. p. 356

[3] Sleeswyk AW, Mandziej S. Mobility of <001> dislocations and formation of cleavage nuclei. Scripta Metallurgica et Materialia. 1990;**24**(1):7

[4] Výrostková A. IMR-SAS, Kosice SK. Case study in COST-538 Action. 2005. Unpublished. Available from: http://www.cost.eu/domains_actions/mpns/Actions/538

[5] Stroh AN. A theory of the fracture of metals. Advances in Physics. 1957;**6**:418

[6] Mandziej ST. Low-energy dislocations and ductility of ferritic steels. Materials Science & Engineering A. 1993;**164**:275

[7] Sleeswyk AW, Mandziej S. Dislocation behaviour in dual-phase steel. In: Kettunen PO et al, editors. Strength of Metals and Alloys. Vol. III. Oxford, UK: Pergamon Press; 1988. p. 155

[8] Lubahn JD, Felgar RP. Plasticity and Creep of Metals. New York: J. Wiley & Sons Inc; 1961

[9] Mandziej ST. Microstructures of heat-affected zones in Cr-Mo-V steels; IIW Doc. II-C-514-17

[10] Gleeble Welding Simulation Brochure 6.12. Poestenkill, USA: DSI; 2016

[11] Mandziej ST. Accelerated creep test for new steels and welds. In: Liu X et al, editors. Energy Materials 2017, The Minerals, Metals & Materials Series. Springer Verlag; 2017. p. 161

[12] Rothwell J, Abson D. Performance of weldments in advanced 9%Cr steel—'FB2'. Materials at High Temperatures. 2010;**27**:253

[13] Kasl J, Jandova D, Kanta V. Behaviour of dissimilar weld joint of steels FB2 and F during long-term creep test. IOP Conference Series: Materials Science and Engineering. 2019;**461**: 012036

[14] Kidin IN. 'Kinetics of Thermal Processes at Different Heating Methods', on p. 42 and 'Electrothermal Treatment of Alloy Steels', on p. 191. In: Fizicheskie Osnovy Elektrotermicheskei Obrabotki Metallov i Splavov (Physical Principles of Electrothermal Treatment of Metals and Alloys). Moscow: Izd. Metallurgia; 1969 (in Russian)

[15] Mandziej ST, Vyrostkova A. Evolution of Cr-Mo-V weld metal microstructure during creep testing— Part 1: P91 material. Welding in the World. 2008;**52**(1–2):3-26

[16] Mandziej ST, Vyrostkova A, Solar M: Evolution of Cr-Mo-V weld metal microstructure during creep testing — Part 2: P24 material. Welding in the World. May 2011;**55**(5-6):52-69

[17] Mandziej ST. ACT study in COST-536 Action. 2005. Unpublished. Available from: http://www.cost.eu/domains actions/mpns/Actions/536

[18] Mandziej ST. Remnant life estimation for repair welding in thermal power generation. In: Design, Fabrication and Economy of Metal Structures, International Conference Proceedings, Miskolc. Hungary: Springer; 2013. p. 263